




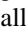



Synthesizing a $\hat{\sigma}_z$ spin-dependent force for optical, metastable, and ground-state trapped-ion qubits

O. Břazavan ^{1,*},† S. Saner ^{1,*},‡ M. Minder ¹ A. C. Hughes ¹ R. T. Sutherland ² D. M. Lucas,¹
R. Srinivas ¹ and C. J. Ballance ^{1,3}

¹*Department of Physics, University of Oxford, Clarendon Laboratory, Parks Road, Oxford OX1 3PU, United Kingdom*

²*Department of Electrical and Computer Engineering, University of Texas at San Antonio, San Antonio, Texas 78249, USA*

³*Oxford Ionics, Oxford OX5 1PF, United Kingdom*



(Received 29 July 2022; accepted 18 November 2022; published 22 February 2023)

A single bichromatic field near resonant to a qubit transition is typically used for $\hat{\sigma}_x$ or $\hat{\sigma}_y$ Mølmer-Sørensen-type interactions in trapped-ion systems. Using this field configuration, it is also possible to synthesize a $\hat{\sigma}_z$ spin-dependent force by merely adjusting the beat-note frequency. Here, we expand on previous work and present a comprehensive theoretical and experimental investigation of this scheme with a laser near resonant to a quadrupole transition in $^{88}\text{Sr}^+$. Further, we characterize its robustness to optical phase and qubit frequency offsets, and demonstrate its versatility by entangling optical, metastable, and ground-state qubits.

DOI: [10.1103/PhysRevA.107.022617](https://doi.org/10.1103/PhysRevA.107.022617)

I. INTRODUCTION

Trapped-ion systems are used for quantum computation [1–3], quantum simulation [4], metrology, and sensing [5,6]. These applications typically require coupling of the internal spin states of the ions to their shared motion via a spin-dependent force (SDF) [7]. These SDFs can arise from the intensity gradient of applied lasers, or from magnetic field gradients [3,8–11]. The basis of the SDF, the specific Pauli spin operator that it corresponds to, depends on its particular physical implementation. For example, time-varying ac Stark shifts can be used to implement $\hat{\sigma}_z$ -type interactions [12–14], while a bichromatic field near resonant to the qubit transition can be used to implement $\hat{\sigma}_x$ or $\hat{\sigma}_y$ Mølmer-Sørensen (MS)-type interactions [15–19]. The basis of the SDF determines the fields required, the applicability of the interaction to different qubit types, and its sensitivity to errors.

The $\hat{\sigma}_z$ -type interaction can be made insensitive to errors from qubit frequency offsets or dephasing, which commute with the interaction [13], using spin-echo sequences [20,21]. This interaction typically requires fields off resonant from the qubit transition and is intrinsically insensitive to phase fluctuations of the driving field. Conventional implementations relying on dipole transitions are incompatible with magnetic-field-insensitive “clock” qubits [22], desirable for their long coherence times [23,24]. Nevertheless, recent experiments have used quadrupole transitions with ground-state qubits [25,26] or dipole transitions with optical qubits [27,28] that enable the interaction to be applied to clock qubits. On the other hand, the MS-type interaction requires near-qubit frequency fields. This interaction is readily applicable to clock qubits, but is sensitive to the phase of the driving field [22,29]. Additionally, the same fields that drive the MS interaction can be tuned to perform single-qubit rotations.

Using near-qubit frequency fields to implement a $\hat{\sigma}_z$ -type interaction minimizes the number of required fields and improves its robustness to errors commuting with the z basis. Moreover, it enables a wider range of interactions, relevant for applications such as quantum simulation [30,31]. Another important consideration is the applicability of a given scheme to a variety of qubit encodings, for example, in the *omg*-type architecture which requires control of optical, metastable, and ground-state qubits [32,33]. Finally, the wavelengths of the required fields also form an important practical criterion. For instance, the wavelengths of quadrupole transitions are usually in the red, which are more favorable for current integrated optics technologies [34,35] and to reduce trap charging effects [36].

In this paper, we investigate a technique for implementing a laser-based $\hat{\sigma}_z$ SDF using a bichromatic field on a quadrupole transition, proposed in Ref. [37] and inspired by recent work in Refs. [38,39] for laser-free interactions. This SDF mechanism was proposed and previously demonstrated using low SDF amplitudes in Refs. [40–42]. We present a comprehensive theoretical treatment of the interaction as well as an in-depth experimental characterization of the SDF for both low and high SDF amplitudes. Moreover, we demonstrate the versatility of the SDF created by using it to entangle optical, metastable, and ground-state qubits.

II. THEORY

To understand this technique, let us first consider a collection of n spins coupled to a motional mode by a bichromatic field [37]. The field is composed of two tones which are symmetrically detuned from the optical qubit frequency, ω_0 , by δ , as shown in Fig. 1(a). These fields give rise to an interaction [16]

$$\hat{H} = \hbar\Omega\hat{S}_{\phi-\pi/2}\cos(\delta t) + \hbar\Omega\eta\hat{S}_{\phi}\cos(\delta t)(\hat{a}e^{-i\omega_z t} + \hat{a}^\dagger e^{i\omega_z t}), \quad (1)$$

*These authors contributed equally to this work.

†oana.bazavan@physics.ox.ac.uk

‡sebastian.saner@physics.ox.ac.uk

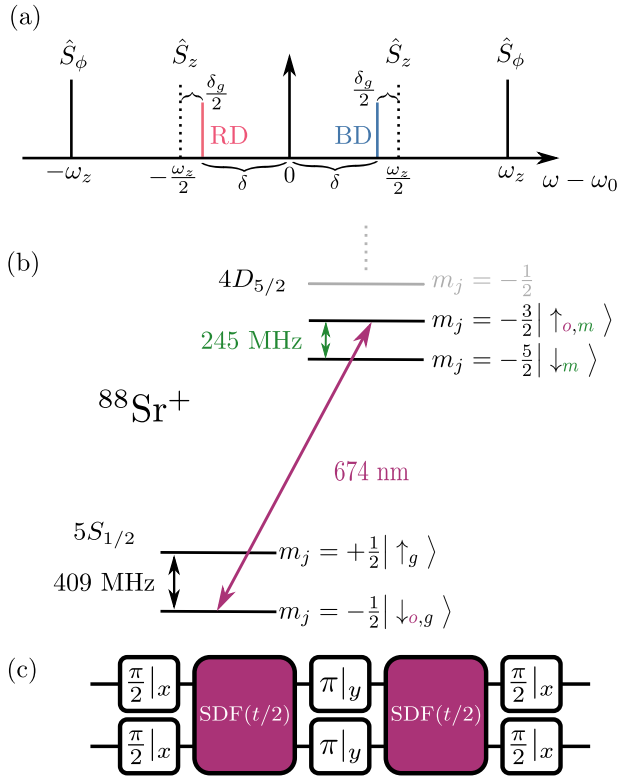


FIG. 1. (a) Frequency configuration of the bichromatic laser field. We apply two 674-nm tones (BD and RD) that are symmetrically detuned from the optical qubit transition frequency ω_0 , by δ . To implement the \hat{S}_z interaction, we set $\delta = (\omega_z - \delta_g)/2$, where δ_g corresponds to the detuning of the effective spin-dependent interaction, and ω_z is the motional mode frequency. (b) Overview of the relevant atomic structure for $^{88}\text{Sr}^+$. Using the same bichromatic field on the 674-nm transition, we implement this scheme on the optical, ($|\downarrow_o\rangle \leftrightarrow |\uparrow_o\rangle$), metastable ($|\downarrow_m\rangle \leftrightarrow |\uparrow_m\rangle$), and ground-state ($|\downarrow_g\rangle \leftrightarrow |\uparrow_g\rangle$) qubits. (c) Pulse sequence for entangling operations. The single-qubit operations (π pulses and $\pi/2$ pulses) are performed with a 674-nm laser for the optical qubit and with a radio-frequency field from an antenna for the ground- and metastable state qubits. The phase of the π pulse is orthogonal to that of the $\pi/2$ pulses.

where Ω denotes the Rabi frequency for each tone and η the Lamb-Dicke factor [3]. The spin operator for n ions is defined as $\hat{S}_\phi = \sum_{i=1}^n \hat{\sigma}_\phi^{(i)}$ with $\hat{\sigma}_\phi^{(i)} = \cos \phi \hat{\sigma}_x^{(i)} + \sin \phi \hat{\sigma}_y^{(i)}$ [43], and \hat{a}^\dagger (\hat{a}) denotes the creation (annihilation) operator of the motional mode. The phase $\phi = (\phi_{\text{BD}} + \phi_{\text{RD}})/2$ is the mean optical phase between the blue-detuned (BD) tones and the red-detuned (RD) tones. The above expression is in the interaction picture with respect to the qubit frequency ω_0 , and the motional mode frequency ω_z , where we applied the rotating-wave approximation with respect to ω_0 . The first term drives spin flips (carrier term) and the second term couples the spins to the motional mode (sideband term). Crucially, these two terms do not commute. The resulting dynamics can be simplified by moving into the interaction picture with respect to the carrier term, details are in Appendix A. Following the

derivation in Refs. [37,38], we obtain

$$\begin{aligned} \hat{H}_I = & \hbar\eta\Omega(\hat{a}e^{-i\omega_z t} + \hat{a}^\dagger e^{i\omega_z t}) \\ & \times \left[\hat{S}_\phi \sum_{n=0}^{\infty} [J_{2n}(2\Omega/\delta) + J_{2n+2}(2\Omega/\delta)] \cos[(2n+1)\delta t] \right. \\ & \left. - \hat{S}_z \sum_{n=1}^{\infty} [J_{2n-1}(2\Omega/\delta) + J_{2n+1}(2\Omega/\delta)] \sin(2n\delta t) \right], \end{aligned} \quad (2)$$

where $\hat{S}_z = \sum_{i=1}^n \hat{\sigma}_z^{(i)}$ and J_n are the Bessel functions of the first kind. Equation (2) reveals an infinite series of resonances which can be selectively driven. In contrast to Ref. [38], here both the carrier and the sideband term oscillate at the same frequency δ , as they originate from the same source. Different choices of δ will drive different interactions; when $\delta \approx \omega_z/(2n+1)$ we drive MS-type interactions, while $\delta \approx \omega_z/(2n)$ corresponds to \hat{S}_z -type interactions. For $\delta \approx \omega_z$, we obtain the conventional MS interaction with coupling strength modulated by $J_0 + J_2$ and a spin-dependent force in the \hat{S}_ϕ basis. However, by choosing $\delta \approx \omega_z/2$, the near-resonant term

$$\begin{aligned} \hat{H}_I = & -\hbar\eta\Omega[J_1(2\Omega/\delta) + J_3(2\Omega/\delta)] \\ & \times \sin(2\delta t)\hat{S}_z(\hat{a}e^{-i\omega_z t} + \hat{a}^\dagger e^{i\omega_z t}) \end{aligned} \quad (3)$$

drives an \hat{S}_z interaction [37] with a coupling strength modulated by $J_1 + J_3$. The effective coupling strength is then $\Omega_{\text{eff}} = \eta\Omega[J_1(2\Omega/\delta) + J_3(2\Omega/\delta)]$. Importantly, this interaction is insensitive to the mean optical phase ϕ of the bichromatic laser field, in contrast to the MS interaction \hat{S}_ϕ . This SDF can be employed for creating entanglement between qubits using standard techniques. Moreover, as this effective \hat{S}_z force is derived from an interaction that couples directly to the qubit levels, it could also be used with field-insensitive “clock” qubits. In the regime where $\Omega \ll \delta$, Eq. (3) reproduces the effective Hamiltonian described in Ref. [40], which was experimentally demonstrated in Refs. [41,42].

III. EXPERIMENTAL IMPLEMENTATION

We experimentally demonstrate this interaction on trapped $^{88}\text{Sr}^+$ ions in a three-dimensional (3D) radio-frequency Paul trap [44,45]. We use a single 674-nm beam with two tones symmetrically detuned from the $|5S_{1/2}, m_j = -\frac{1}{2}\rangle \leftrightarrow |4D_{5/2}, m_j = -\frac{3}{2}\rangle$ quadrupole transition at a 146 G magnetic field. For both the single- and two-ion experiments, we choose to drive the axial in-phase mode with $\omega_z/2\pi \approx 1.2$ MHz. We obtain carrier Rabi frequencies of $\Omega/2\pi = 0.14\text{--}1.17$ MHz using a beam waist radius of 20 μm and laser powers between 0.5 and 35 mW. To generate the SDF acting in the \hat{S}_z basis, we set $\delta = (\omega_z - \delta_g)/2$ as shown in Fig. 1(a), where δ_g is the detuning of the $\hat{\sigma}_z$ interaction from resonance. Unless stated otherwise, the pulses generating the \hat{S}_z interaction are embedded in a spin-echo Ramsey sequence [20,21] [see Fig. 1(c)]. We set the phase of the SDF in the second pulse to match the phase of the SDF at the beginning of the first pulse relative to the ion motion. To transition smoothly into the bichromatic interaction picture, we ramp the bichromatic field on and off with a \sin^2 ramp shape. The

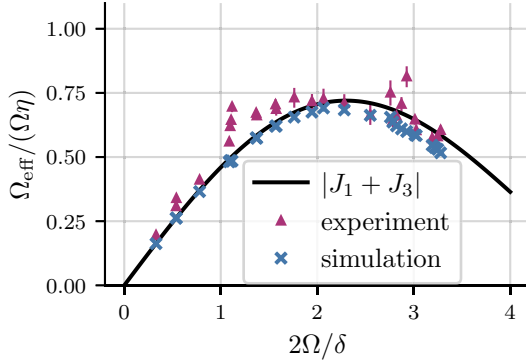


FIG. 2. Spin-dependent force strength Ω_{eff} , normalized by $\Omega\eta$ (see text), vs $2\Omega/\delta$, as measured on a single ion, with $\delta \approx \omega_z/2$. We show the experimental data (magenta triangles) extracted from measuring the spin-dependent force amplitude by applying the interaction for variable durations and fitting the dynamics (Appendix B 1). The error bars are inferred from the fits, showing 68% confidence intervals. The data agree with the theory, $|J_1(2\Omega/\delta) + J_3(2\Omega/\delta)|$ (black line). To validate the approximations in Eq. (3) we perform numerical simulations of Eq. (1) (blue crosses), using the experimental parameters, and we follow the same extraction procedure for Ω_{eff} as for the measured data.

ramp duration should be long compared to $1/\delta$, which is approximately 2 μs . We use ramp durations of 5 or 10 μs .

We experimentally verify two important characteristics of the SDF using the optical qubit states $|\downarrow_o\rangle \equiv |5S_{1/2}, m_j = -\frac{1}{2}\rangle$ and $|\uparrow_o\rangle \equiv |4D_{5/2}, m_j = -\frac{3}{2}\rangle$, on a single ion. First, we show that the SDF magnitude follows the predicted Bessel function dependence, $J_1(2\Omega/\delta) + J_3(2\Omega/\delta)$ (see Fig. 2). For each data point, we apply the sequence shown in Fig. 1(c) to a single qubit and measure the single-ion population as a function of the SDF pulse duration t . We fit these dynamics to an effective SDF model with magnitude Ω_{eff} , normalized by Ω and the Lamb-Dicke factor $\eta \approx 0.054$, which are independently determined (Appendix B 1). We repeat the experiment for different values of $2\Omega/\delta$ by changing both the Rabi frequency Ω and detuning δ . We also perform numerical simulations of Eq. (1), assuming the experimental parameters and applying the same method for extracting Ω_{eff} . For larger values of $2\Omega/\delta$ the numerical simulation deviates from the theory curve, which does not include any dynamics during the ramp.

Second, we verify that the SDF acts in the \hat{S}_z basis and compare it to the MS case. We embed the SDF in a sequence similar to Fig. 1(c), applied to a single qubit, but omit the π pulse, and the second SDF pulse. Then, we scan the phase ϕ_0 of both the $\pi/2$ pulses relative to the SDF drive (Fig. 3). Changing ϕ_0 modifies the initial superposition of the spin states; the SDF acting on its eigenstate will effect no spin-dependent displacement. We map the generated spin-dependent displacement onto the spin state and measure the population p_\uparrow in $|\uparrow_o\rangle$. We set the detuning and duration of the SDF to generate a large enough spin-dependent displacement such that $p_\uparrow \approx 0.5$. For this scheme, p_\uparrow is independent of ϕ_0 . Hence, the SDF basis is orthogonal to the \hat{S}_x - \hat{S}_y plane and corresponds to \hat{S}_z . In contrast, for the MS-type interaction, which acts in the \hat{S}_ϕ basis, the spin-dependent displacement

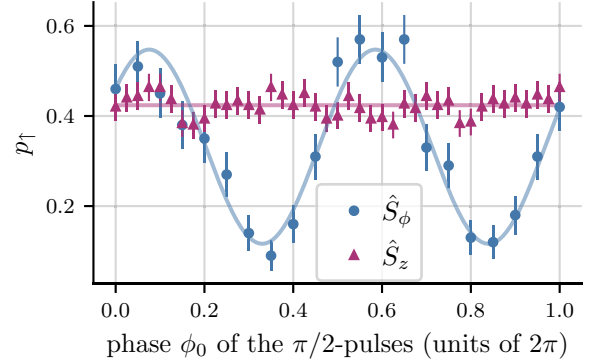


FIG. 3. Verification of the spin-dependent force (SDF) basis. We scan the phase ϕ_0 of the $\pi/2$ pulses relative to the SDF. We map the spin-dependent displacement generated by both \hat{S}_z (magenta triangles) and \hat{S}_ϕ (blue circles) forces onto $|\uparrow_o\rangle$ and measure the population p_\uparrow (see text). As expected, the signal for the \hat{S}_z SDF has no dependence on ϕ_0 , while the \hat{S}_ϕ SDF does. The solid lines are a guide to the eye of the expected dependence. Error bars indicate 68% confidence intervals.

depends on whether the superposition state after the first $\pi/2$ pulse is aligned or orthogonal to the SDF basis. In these experiments, we switch the basis of the force by setting the detuning to $\delta \approx \omega_z/2$ or $\delta \approx \omega_z$ for the \hat{S}_z or \hat{S}_ϕ interactions, respectively.

Another important aspect of this \hat{S}_z force is its suitability to any qubit encoding where one or both qubit levels are part of the quadrupole transition used to generate the SDF, as these states are all eigenstates of the interaction. This property does not hold for the \hat{S}_ϕ case. We demonstrate the versatility of this SDF by implementing a geometric-phase two-qubit \hat{S}_z entangling gate on the optical, metastable, and ground-state qubits following the pulse sequence in Fig. 1(c). The experimental parameters for Ω and δ for all three demonstrations correspond to $2\Omega/\delta \approx 1.6$, the argument of the Bessel function in Fig. 2. The quoted gate durations correspond to $4\pi/\delta_g$. The total duration of the SDF pulses includes an additional 20 μs for the ramps. For each of the qubit types, we create the entangled state $\frac{1}{\sqrt{2}}(|\downarrow\downarrow\rangle + |\uparrow\uparrow\rangle)$. We infer the fidelity of the created Bell state by measuring the populations and the parity, $1 - 2(p_{\uparrow\downarrow} + p_{\downarrow\uparrow})$. For the parity measurement, we add a $\pi/2$ analysis pulse with a variable phase [17] after the pulse sequence in Fig. 1(c). We report the fidelity \mathcal{F} without correcting for any state preparation and measurement (SPAM) error $\bar{\epsilon}$ [46]. We separately quote $\bar{\epsilon}$ as measured for two ions.

A. Optical qubit

We start with the optical qubit, where the SDF couples to both qubit states $|\downarrow_o\rangle$ and $|\uparrow_o\rangle$. We obtain a Bell-state fidelity of $\mathcal{F} = 0.930(3)$ for a gate duration of $\approx 70 \mu\text{s}$ at 9.1 mW. The SPAM error is $\bar{\epsilon} = 0.0016(2)$. An example parity scan is shown in Fig. 4. In contrast to MS-gate implementations, the phase of the entangled state is fixed and does not depend on the average phase of the two bichromatic field tones. The SDF pulses and the single-qubit rotations were implemented using the same 674-nm laser.

To demonstrate the robustness of the gate mechanism to $\hat{\sigma}_z$ -type errors, we measure the Bell-state fidelity as a function

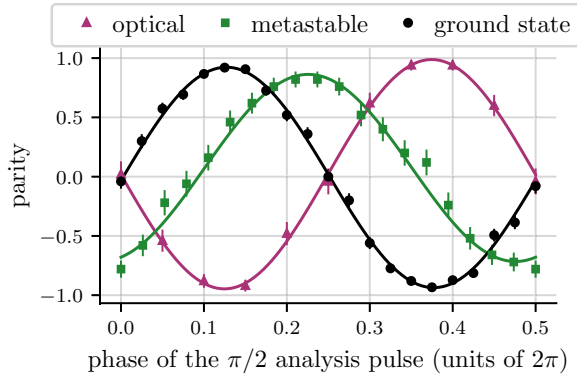


FIG. 4. Example parity scans for two-qubit entangled states created in the optical (magenta triangles), metastable (green squares), and ground-state (black circles) qubits. We scan the $\pi/2$ analysis pulse phase and measure the parity (see text). Error bars indicate 68% confidence intervals, and lines are fits to the data.

of an applied qubit frequency offset, where we shift both tones by the same offset, during the gate pulses (Fig. 5). From -150 to 150 kHz, the Bell-state fidelity values are statistically consistent with each other and stay above 0.9.

B. Metastable qubit

We next entangle the metastable qubit states $|\downarrow_m\rangle \equiv |4D_{5/2}, m_j = -\frac{5}{2}\rangle$ and $|\uparrow_m\rangle \equiv |4D_{5/2}, m_j = -\frac{3}{2}\rangle$, split by ≈ 245 MHz [see Fig. 1(b)]. We obtain a Bell-state fidelity of $\mathcal{F} = 0.859(5)$ for a gate duration of ≈ 140 μ s at 9.5 mW laser power. The SPAM error is $\bar{\epsilon} = 0.0164(7)$. As the SDF only couples to the $|\uparrow_m\rangle$ state, the differential force between the qubit states is half that of the optical qubit. Hence, the gate duration is about twice as long as for the optical qubit case using similar laser power. The single-qubit rotations for the metastable qubit are performed with a radio-frequency (rf) antenna; crucially we require no defined phase relationship between the rf source and the 674-nm laser for the SDF.

As the Zeeman splitting between neighboring $4D_{5/2}$ states is almost identical, the qubit states need to be isolated to prevent population leakage during the single-qubit rotations. To break the degeneracy, we light shift the $|\uparrow_m\rangle$ level by applying

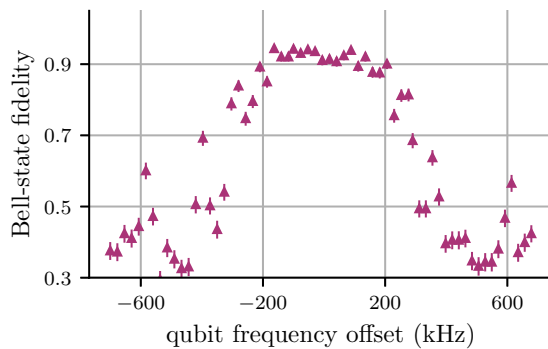


FIG. 5. Bell-state fidelity \mathcal{F} vs the applied qubit frequency offset for the optical qubit. The Bell-state fidelity remains unchanged above 0.9 over a range of ± 150 kHz. Fidelity values below 0.5 indicate a change in the phase of the created Bell state.

a 674-nm beam blue detuned from the optical quadrupole transition ($|\downarrow_o\rangle \leftrightarrow |\uparrow_o\rangle = |\uparrow_m\rangle$) during the single-qubit rotations. Using a detuning of 2.8 MHz and power of 20 mW, we shift the qubit transition by ≈ 145 kHz from the neighboring transition. We attribute most of the additional infidelity compared to the optical qubit case to imperfect state initialization and single-qubit rotations. We show a sample parity scan for the metastable qubit in Fig. 4. The detuned 674-nm field used during the single-qubit operations also induces a phase shift on the entangled state which results in a phase offset in the parity scan.

C. Ground-state qubit

Finally, we demonstrate a two-qubit entangling gate using the ground-state qubits $|\downarrow_g\rangle \equiv |5S_{1/2}, m_j = -\frac{1}{2}\rangle$ and $|\uparrow_g\rangle \equiv |5S_{1/2}, m_j = \frac{1}{2}\rangle$, split by 409 MHz [see Fig. 1(b)]. We obtain a Bell-state fidelity of $\mathcal{F} = 0.949(4)$ for a gate duration of ≈ 140 μ s at 9 mW laser power. The SPAM error is $\bar{\epsilon} = 0.0036(4)$. Similarly, the single-qubit rotations are implemented via the rf antenna. Again, the gate duration is doubled compared to the optical qubit case as the SDF only couples to $|\downarrow_g\rangle$.

IV. DISCUSSION

We have shown that the technique is applicable to three different qubit types using the exact same bichromatic field. Within the context of *omg* architectures, this simplifies the technical requirements as it enables the manipulation of all three qubit encodings using a single quadrupole laser. However, there might be additional considerations for multi-ion chains. For example, a global laser beam would couple ions whose qubits are either in the ground or metastable manifold. Single-ion addressing of the gate drive preserves orthogonality in the qubit subspace. However, most *omg* applications would require single-ion addressing which would mitigate this issue. In addition, auxiliary states in either manifold that do not couple to the bichromatic field can be used to shelve quantum states temporarily. Another application of this scheme, not explored in this paper, is entangling ions that use different qubits, e.g., metastable–ground state, optical–ground state.

In terms of the errors associated with the entangling operations using this SDF scheme, we are able to achieve Bell-state fidelities comparable to those achieved by the MS interaction in the same system. We believe the main sources of infidelity are phase noise from the 674-nm laser and excitation of other motional mode resonances. The phase of the entangled state, and hence the fidelity, is insensitive to slow drifts in the optical phase for the \hat{S}_z interaction. However, similar to the MS interaction, it is still sensitive to phase noise that is fast compared to the duration of an entangling gate. Additionally, single-qubit rotations on the optical qubit can also induce errors. We observed a loss in contrast from the spin-echo Ramsey sequences [Fig. 1(c)] without any SDF pulses at delays close to the durations used for the entangling gates. The contrast loss on the two-ion population $p_{\uparrow\downarrow} + p_{\downarrow\uparrow}$ was 0.035(3) for the optical qubit encoding. This indicates the presence of colored phase noise on the 674-nm laser which could significantly affect the gate dynamics. For the ground-state and the

metastable qubit, the contrast loss was dominated by SPAM errors. Furthermore, there are additional resonances close to $\delta \approx \omega_z/2$ as the laser couples to all the motional modes of the ions (Appendix B 2). We observed that sideband cooling of the additional motional modes corresponding to these nearby resonances mitigates this error contribution.

V. CONCLUSION

In conclusion, we present an in-depth investigation of a spin-dependent force in the $\hat{\sigma}_z$ basis created using a bichromatic laser-field near resonant with a quadrupole transition. By only changing the beat-note frequency of the near-qubit tones, we can toggle the interaction basis from the typical $\hat{\sigma}_\phi$ to $\hat{\sigma}_z$. We characterize this interaction and investigate its robustness to $\hat{\sigma}_z$ -type errors, such as qubit frequency offsets, and show that the basis of the SDF does not depend on the optical phase of the driving field. This SDF is well suited to manipulate a variety of qubit states. We use the same laser configuration to entangle optical, metastable, and ground-state qubits, which is important for recently proposed trapped-ion architectures [32,33]. While demonstrated for field-sensitive transitions (there are no clock qubits in $^{88}\text{Sr}^+$), this method could be extended to field-insensitive clock qubits. Moving beyond quadrupole transitions, this method can also be used with two-photon Raman and magnetic dipole transitions in other trapped-ion systems.

ACKNOWLEDGMENTS

We thank David Allcock, Gabriel Araneda, and Alejandro Bermúdez for comments on the manuscript. This work was

supported by the U.K. EPSRC Hub in Quantum Computing and Simulation (EP/T001062/1) and the U.S. Army Research Office (W911NF-20-1-0038).

APPENDIX A: DERIVATION OF $\hat{\sigma}_z$ INTERACTION

In this section, we present a more general form of Eq. (1) and show an intermediate step in the derivation of Eq. (2). As in the main text, we start with the Hamiltonian that describes the coupling of a bichromatic field with a beat-note frequency 2δ and n spins

$$\hat{H} = \hbar\Omega\hat{S}_{\phi-\pi/2}\cos(\delta t - \zeta) + \hbar\Omega\eta\hat{S}_\phi\cos(\delta t - \zeta)(\hat{a}e^{-i\omega_z t} + \hat{a}^\dagger e^{i\omega_z t}), \quad (\text{A1})$$

where Ω denotes the Rabi frequency for each tone and η the Lamb Dicke factor [3]. The spin operator for n ions is defined as $\hat{S}_\phi = \sum_{i=1}^n \hat{\sigma}_\phi^{(i)}$ with $\hat{\sigma}_\phi^{(i)} = \cos\phi\hat{\sigma}_x^{(i)} + \sin\phi\hat{\sigma}_y^{(i)}$, and \hat{a}^\dagger (\hat{a}) denotes the creation (annihilation) operator of the motional mode. The phase $\phi = (\phi_{\text{BD}} + \phi_{\text{RD}})/2$ is the mean optical phase between the blue-detuned (BD) tones and the red-detuned (RD) tones. Here, we also include the phase $\zeta = (\phi_{\text{BD}} - \phi_{\text{RD}})/2$, the difference in optical phase between the two tones. In our field configuration, we have control over ζ while ϕ is drifting. The above expression is in the interaction picture with respect to the qubit frequency ω_0 and the motional mode frequency ω_z , where we applied the rotating wave approximation with respect to ω_0 . We express the Hamiltonian in the interaction picture with respect to the carrier coupling $\hbar\Omega\hat{S}_{\phi-\pi/2}\cos(\delta t - \zeta)$ and we use $[\hat{S}_{\phi-\pi/2}, \hat{S}_\phi] = i\hat{S}_z$ to obtain

$$\hat{H}_I = \hbar\eta\Omega\cos(\delta t - \zeta)(\hat{a}e^{-i\omega_z t} + \hat{a}^\dagger e^{i\omega_z t}) \left[\hat{S}_\phi \left(J_0(2\Omega/\delta) + 2 \sum_{n=1}^{\infty} J_{2n}(2\Omega/\delta)\cos(2n(\delta t - \zeta)) \right) - 2\hat{S}_z \sum_{n=1}^{\infty} J_{2n-1}(2\Omega/\delta)\sin((2n-1)(\delta t - \zeta)) \right], \quad (\text{A2})$$

as shown in Refs. [37,38]. Simplifying Eq. (A2) further, the Hamiltonian is

$$\hat{H}_I = \hbar\eta\Omega(\hat{a}e^{-i\omega_z t} + \hat{a}^\dagger e^{i\omega_z t}) \left[\hat{S}_\phi \sum_{n=0}^{\infty} (J_{2n}(2\Omega/\delta) + J_{2n+2}(2\Omega/\delta))\cos((2n+1)(\delta t - \zeta)) - \hat{S}_z \sum_{n=1}^{\infty} (J_{2n-1}(2\Omega/\delta) + J_{2n+1}(2\Omega/\delta))\sin(2n(\delta t - \zeta)) \right]. \quad (\text{A3})$$

By setting $\delta \approx \omega_z/2$, the leading term is

$$\hat{H}_I \approx -\hbar\eta\Omega(J_1(2\Omega/\delta) + J_3(2\Omega/\delta)) \times \sin(2(\delta t - \zeta))\hat{S}_z(\hat{a}e^{-i\omega_z t} + \hat{a}^\dagger e^{i\omega_z t}), \quad (\text{A4})$$

which corresponds to a $\hat{\sigma}_z$ SDF [37]. In the main text, we set $\zeta = 0$ for simplicity. In practice, we adjust ζ such that the phase of the SDF for the second pulse matches the phase of the SDF of the first pulse relative to the ion motion.

APPENDIX B: EXPERIMENTAL DETAILS

1. Spin-dependent force extraction

For each data point in Fig. 2, we apply the SDF to a single ion and measure the population p_\uparrow as a function of the SDF duration, as shown in Fig. 6. We fit these dynamics to obtain the magnitude of the SDF, Ω_{eff} . We use an effective SDF model [29], which is described by

$$\hat{H}_{\text{eff}} = \hbar\Omega_{\text{eff}}(t)(\hat{a}e^{-i\delta_{\text{eff}} t} + \hat{a}^\dagger e^{i\delta_{\text{eff}} t})\hat{S}_z, \quad (\text{B1})$$

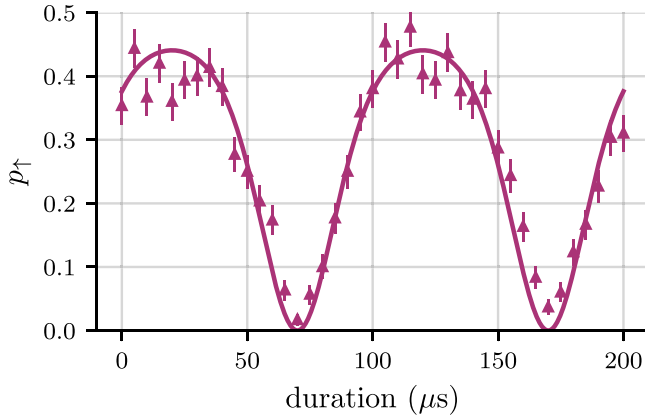


FIG. 6. Example dynamics of the SDF applied to a single ion in the optical qubit. We plot the population of the ion in the $|\uparrow\rangle$ as a function of the pulse duration. For this scan, $2\Omega/\delta \approx 1.1$. Error bars indicate 68% confidence intervals, and the line is a fit to the data following Eq. (B1).

where the Rabi frequency of the interaction $\Omega(t)$ follows

$$\Omega(t) = \begin{cases} \Omega_{\text{eff}} \sin\left(\frac{\pi}{2} \frac{t}{t_{\text{ramp}}}\right)^2, & t < t_{\text{ramp}} \\ \Omega_{\text{eff}}, & t_{\text{ramp}} \leq t \leq t_{\text{total}} - t_{\text{ramp}} \\ \Omega_{\text{eff}} \sin\left(\frac{\pi}{2} \frac{t_{\text{total}} - t}{t_{\text{ramp}}}\right)^2, & t > t_{\text{total}} - t_{\text{ramp}}, \end{cases} \quad (\text{B2})$$

where t_{total} is the total duration of a single SDF pulse including the ramps. The duration over which the SDF is turned on and off is described by t_{ramp} . The SDF described in Eq. (B1) gives rise to a spin-dependent displacement $\hat{U}(t) = \hat{D}(\alpha(t))|\uparrow\rangle\langle\uparrow| + \hat{D}(-\alpha(t))|\downarrow\rangle\langle\downarrow|$, where $\alpha(t) \propto \Omega(t)(1 - e^{-\delta_g t})$. We integrate $\alpha(t)$, keeping t_{ramp} and δ_g fixed. For the fit, we also take into consideration the initial thermal occupation of $\bar{n} \approx 0.1$, measured through sideband asymmetry. In our 3D Paul trap, the heating rate for this motional mode is $\dot{\bar{n}} \approx 35$ quanta/s. We do not include heating in the fitting model as it has a negligible effect on the dynamics.

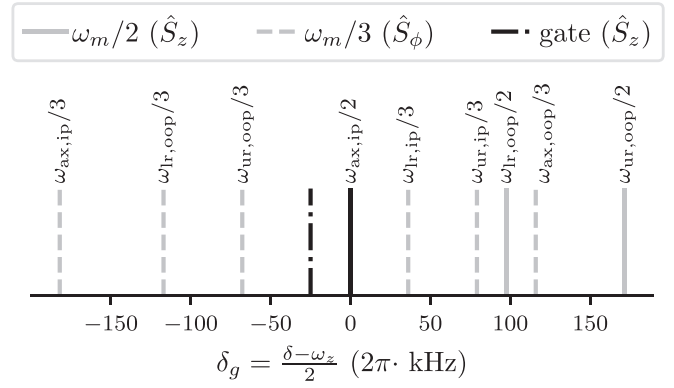


FIG. 7. Spectrum of spectator resonances. The two-qubit \hat{S}_z gate is performed on the axial in-phase mode ($\omega_z = \omega_{\text{ax,ip}}$). The interaction resonance frequency and the detuning used for the gate are indicated by the solid black line and the dash-dotted black line, respectively. The other resonances are annotated with the motional mode abbreviation that they correspond to: axial out-of-phase ($\omega_{\text{ax,oop}}$), lower radial in-phase ($\omega_{\text{lr,ip}}$), upper radial in-phase ($\omega_{\text{ur,ip}}$), lower radial out-of-phase ($\omega_{\text{lr,oop}}$), upper radial out-of-phase ($\omega_{\text{ur,oop}}$). Solid grey lines denote \hat{S}_z couplings ($\delta \approx \omega_m/2$) and dashed grey lines denote \hat{S}_ϕ couplings ($\delta \approx \omega_m/3$).

2. Spectator modes

In our system, the 674 nm laser has a projection on all three trap axes. Hence for a two-ion crystal, the laser couples to all six motional modes. The motional modes are the axial in-phase ($\omega_{\text{ax,ip}}$), axial out-of-phase ($\omega_{\text{ax,oop}}$), lower radial in-phase ($\omega_{\text{lr,ip}}$), upper radial in-phase ($\omega_{\text{ur,ip}}$), lower radial out-of-phase ($\omega_{\text{lr,oop}}$), upper radial out-of-phase ($\omega_{\text{ur,oop}}$). Their frequencies are $\{\omega_{\text{ax,ip}}, \omega_{\text{ax,oop}}, \omega_{\text{lr,ip}}, \omega_{\text{ur,ip}}, \omega_{\text{lr,oop}}, \omega_{\text{ur,oop}}\}/2\pi = \{1.2, 2.0, 1.7, 1.9, 1.3, 1.4\}$ MHz (see Fig. 7). The gate was performed on the axial in-phase mode ($\omega_z = \omega_{\text{ax,ip}}$). All mode resonances in the vicinity of δ will be spectators of the interaction. The dynamics are governed by Eq. (2) with the respective mode frequency and Lamb Dicke parameter. Any residual population $p_{\uparrow\downarrow} + p_{\downarrow\uparrow}$ at the end of the gate sequence will result in an error. By sideband cooling the lower radial in-phase, upper radial out-of-phase, axial out-of-phase, and axial in-phase in that order instead of only cooling the axial modes, we observe a decrease in $p_{\uparrow\downarrow} + p_{\downarrow\uparrow}$ from ≈ 0.08 to ≈ 0.04 .

[1] J. I. Cirac and P. Zoller, *Phys. Rev. Lett.* **74**, 4091 (1995).
[2] C. Monroe, D. M. Meekhof, B. E. King, W. M. Itano, and D. J. Wineland, *Phys. Rev. Lett.* **75**, 4714 (1995).
[3] D. J. Wineland, C. Monroe, W. M. Itano, D. Leibfried, B. E. King, and D. M. Meekhof, *J. Res. Natl. Inst. Stand. Technol.* **103**, 259 (1998).
[4] R. Blatt and C. F. Roos, *Nat. Phys.* **8**, 277 (2012).
[5] P. O. Schmidt, T. Rosenband, C. Langer, W. M. Itano, J. C. Bergquist, and D. J. Wineland, *Science* **309**, 749 (2005).
[6] F. Wolf, Y. Wan, J. C. Heip, F. Gebert, C. Shi, and P. O. Schmidt, *Nature (London)* **530**, 457 (2016).
[7] R. Blatt and D. Wineland, *Nature (London)* **453**, 1008 (2008).

[8] F. Mintert and C. Wunderlich, *Phys. Rev. Lett.* **87**, 257904 (2001).
[9] C. Ospelkaus, C. E. Langer, J. M. Amini, K. R. Brown, D. Leibfried, and D. J. Wineland, *Phys. Rev. Lett.* **101**, 090502 (2008).
[10] M. Johanning, A. Braun, N. Timoney, V. Elman, W. Neuhauser, and C. Wunderlich, *Phys. Rev. Lett.* **102**, 073004 (2009).
[11] C. Ospelkaus, U. Warring, Y. Colombe, K. Brown, J. M. Amini, D. Leibfried, and D. J. Wineland, *Nature (London)* **476**, 181 (2011).
[12] G. J. Milburn, S. Schneider, and D. F. V. James, *Fortschr. Phys.* **48**, 801 (2000).

- [13] D. Leibfried, B. DeMarco, V. Meyer, D. Lucas, M. Barrett, J. Britton, W. M. Itano, B. Jelenković, C. Langer, T. Rosenband, and D. J. Wineland, *Nature (London)* **422**, 412 (2003).
- [14] C. J. Ballance, T. P. Harty, N. M. Linke, M. A. Sepiol, and D. M. Lucas, *Phys. Rev. Lett.* **117**, 060504 (2016).
- [15] A. Sørensen and K. Mølmer, *Phys. Rev. Lett.* **82**, 1971 (1999).
- [16] A. Sørensen and K. Mølmer, *Phys. Rev. A* **62**, 022311 (2000).
- [17] C. A. Sackett, D. Kielpinski, B. E. King, C. Langer, V. Meyer, C. J. Myatt, M. Rowe, Q. Turchette, W. M. Itano, D. J. Wineland, and C. Monroe, *Nature (London)* **404**, 256 (2000).
- [18] J. P. Gaebler, T. R. Tan, Y. Lin, Y. Wan, R. Bowler, A. C. Keith, S. Glancy, K. Coakley, E. Knill, D. Leibfried, and D. J. Wineland, *Phys. Rev. Lett.* **117**, 060505 (2016).
- [19] A. Erhard, J. J. Wallman, L. Postler, M. Meth, R. Stricker, E. A. Martinez, P. Schindler, T. Monz, J. Emerson, and R. Blatt, *Nat. Commun.* **10**, 5347 (2019).
- [20] E. L. Hahn, *Phys. Rev.* **80**, 580 (1950).
- [21] M. H. Levitt, *Prog. Nucl. Magn. Reson. Spectrosc.* **18**, 61 (1986).
- [22] P. J. Lee, K.-A. Brickman, L. Deslauriers, P. C. Haljan, L.-M. Duan, and C. Monroe, *J. Opt. B: Quantum Semiclass. Opt.* **7**, S371 (2005).
- [23] C. Langer, R. Ozeri, J. D. Jost, J. Chiaverini, B. DeMarco, A. Ben-Kish, R. B. Blakestad, J. Britton, D. B. Hume, W. M. Itano, D. Leibfried, R. Reichle, T. Rosenband, T. Schaetz, P. O. Schmidt, and D. J. Wineland, *Phys. Rev. Lett.* **95**, 060502 (2005).
- [24] P. Wang, C.-Y. Luan, M. Qiao, M. Um, J. Zhang, Y. Wang, X. Yuan, M. Gu, J. Zhang, and K. Kim, *Nat. Commun.* **12**, 233 (2021).
- [25] L. Aolita, K. Kim, J. Benhelm, C. F. Roos, and H. Häffner, *Phys. Rev. A* **76**, 040303(R) (2007).
- [26] C. H. Baldwin, B. J. Bjork, M. Foss-Feig, J. P. Gaebler, D. Hayes, M. G. Kokish, C. Langer, J. A. Sedlacek, D. Stack, and G. Vittorini, *Phys. Rev. A* **103**, 012603 (2021).
- [27] B. C. Sawyer and K. R. Brown, *Phys. Rev. A* **103**, 022427 (2021).
- [28] C. R. Clark, H. N. Tinkey, B. C. Sawyer, A. M. Meier, K. A. Burkhardt, C. M. Seck, C. M. Shappert, N. D. Guise, C. E. Volin, S. D. Fallek, H. T. Hayden, W. G. Rellergert, and K. R. Brown, *Phys. Rev. Lett.* **127**, 130505 (2021).
- [29] P. C. Haljan, K.-A. Brickman, L. Deslauriers, P. J. Lee, and C. Monroe, *Phys. Rev. Lett.* **94**, 153602 (2005).
- [30] J. W. Britton, B. C. Sawyer, A. C. Keith, C.-C. J. Wang, J. K. Freericks, H. Uys, M. J. Biercuk, and J. J. Bollinger, *Nature (London)* **484**, 489 (2012).
- [31] A. Bermudez, L. Tagliacozzo, G. Sierra, and P. Richerme, *Phys. Rev. B* **95**, 024431 (2017).
- [32] H.-X. Yang, J.-Y. Ma, Y.-K. Wu, Y. Wang, M.-M. Cao, W.-X. Guo, Y.-Y. Huang, L. Feng, Z.-C. Zhou, and L.-M. Duan, *Nat. Phys.* **18**, 1058 (2022).
- [33] D. T. C. Allcock, W. C. Campbell, J. Chiaverini, I. L. Chuang, E. R. Hudson, I. D. Moore, A. Ransford, C. Roman, J. M. Sage, and D. J. Wineland, *Appl. Phys. Lett.* **119**, 214002 (2021).
- [34] R. J. Niffenegger, J. Stuart, C. Sorace-Agaskar, D. Kharas, S. Bramhavar, C. D. Bruzewicz, W. Loh, R. T. Maxson, R. McConnell, D. Reens, G. N. West, J. M. Sage, and J. Chiaverini, *Nature (London)* **586**, 538 (2020).
- [35] K. K. Mehta, C. Zhang, M. Malinowski, T.-L. Nguyen, M. Stadler, and J. P. Home, *Nature (London)* **586**, 533 (2020).
- [36] S. X. Wang, G. Hao Low, N. S. Lachenmyer, Y. Ge, P. F. Herskind, and I. L. Chuang, *J. Appl. Phys.* **110**, 104901 (2011).
- [37] C. F. Roos, *New J. Phys.* **10**, 013002 (2008).
- [38] R. T. Sutherland, R. Srinivas, S. C. Burd, D. Leibfried, A. C. Wilson, D. J. Wineland, D. T. C. Allcock, D. H. Slichter, and S. B. Libby, *New J. Phys.* **21**, 033033 (2019).
- [39] R. Srinivas, S. C. Burd, H. M. Knaack, R. T. Sutherland, A. Kwiatkowski, S. Glancy, E. Knill, D. J. Wineland, D. Leibfried, A. C. Wilson, D. T. C. Allcock, and D. H. Slichter, *Nature (London)* **597**, 209 (2021).
- [40] K. Kim, C. F. Roos, L. Aolita, H. Häffner, V. Nebendahl, and R. Blatt, *Phys. Rev. A* **77**, 050303(R) (2008).
- [41] T. Monz, K. Kim, A. S. Villar, P. Schindler, M. Chwalla, M. Riebe, C. F. Roos, H. Häffner, W. Hänsel, M. Hennrich, and R. Blatt, *Phys. Rev. Lett.* **103**, 200503 (2009).
- [42] D. J. Gorman, B. Hemmerling, E. Megidish, S. A. Moeller, P. Schindler, M. Sarovar, and H. Häffner, *Phys. Rev. X* **8**, 011038 (2018).
- [43] $\hat{\sigma}_{x,y}^{(i)} = \underbrace{\hat{\mathbb{I}}_2 \otimes \cdots \otimes \hat{\mathbb{I}}_2}_{i-1} \otimes \hat{\sigma}_{x,y} \otimes \underbrace{\hat{\mathbb{I}}_2 \otimes \cdots \otimes \hat{\mathbb{I}}_2}_{n-i}$.
- [44] V. Schäfer, Fast gates and mixed-species entanglement with trapped ions, Ph.D. thesis, University of Oxford, 2018.
- [45] K. Thirumalai, High-fidelity mixed species entanglement of trapped ions, Ph.D. thesis, University of Oxford, 2019.
- [46] C. J. Ballance, *High-Fidelity Quantum Logic in Ca+* (Springer, Berlin, 2017).